Microstructural modification of recycled aluminium alloys by high-intensity ultrasonication: observations from custom Al-2Si-2Mg-1.2Fe-(0.5,1.0)Mn alloys

H.R. Kotadia[a], M. Qian[b], A. Das[c,*]

[a] Warwick Manufacturing Group, The University of Warwick, Coventry CV4 7AL, UK

[b] School of Engineering, RMIT University, Melbourne, VIC 3000, Australia

[c] Materials Research Centre, College of Engineering, Swansea University Bay Campus, Fabian Way, Swansea, SA1 8EN, UK

Abstract

The effect of ultrasonication on the solidification microstructure of recycled Al-alloys is investigated using custom Al-2Si-2Mg-1.2Fe-xMn alloys (x = 0.5 and 1%, in wt.%) through cooling curve measurement, optical and electron microscopy, X-ray diffraction, differential scanning calorimetry and computational thermodynamic calculations. Applying ultrasonication throughout the primary-Al nucleation stage resulted in refined non-dendritic grain structure. Cooling curves indicate a noticeable reduction in primary-Al nucleation undercooling and reduction of the recalescence peak under ultrasonication. However, terminating ultrasonication prior to the nucleation of primary-Al led to dendritic grains with marginal refinement. Without ultrasonication, coarse Chinese-script $\alpha-Al_{15}(Fe,Mn)_3Si_2$ intermetallics developed from initially polygonal particles due to interface growth instability under thermo-solutal undercooling. In contrast, ultrasonication produced refined and polygonal $\alpha-Al_{15}(Fe,Mn)_3Si_2$ particles by promoting nucleation and growth stabilisation under strong fluid flow. The enhanced nucleation from ultrasonication is presumably due to the pressure-induced shift of freezing point along with improved wetting of insoluble inclusions under cavitation. The present results show that ultrasonication can effectively modify the Fe-intermetallics and refine the grain structure in recycled Al-alloys.

* Corresponding author. Tel.: +44 1792 602031 E-mail address: A.Das@swansea.ac.uk (A. Das)

1. Introduction

Tailoring solidification microstructure is an important means to control the mechanical properties or downstream processability of Al-alloys. Solidification microstructure in Al-alloys can involve a complex combination of intermetallic phases with the primary-Al grains and eutectic phases. Grain refinement [1-2] and eutectic modification [3-4] through chemical means are widely practiced to improve the solidification microstructure, mechanical property and processability of Al-alloys. Secondary processing (recycling), though desirable (see below), further complicates the microstructure evolution due to the formation of Fe-containing intermetallic phases that are often detrimental to the performance of the alloys.

Recycling of aluminium has significant environmental and economic benefits over primary production, stemming largely from a substantial (~ 95%) reduction in the energy requirement [5-7]. However, the accumulation of impurities and tramp elements is difficult to avoid. Their removal from the Al-melt is energy intensive and severely limited for thermodynamic reasons [5, 8-9]. The most detrimental and pervasive impurity is Fe that is picked up from the ores, master alloys and recycled scrap as well as through contamination from ferrous tools during manufacturing [10-11]. Most commercial aluminium alloys have iron impurity around 0.2 wt.%, which increases further to a level of 0.3–0.8 wt.% or even higher during recycling [10]. The presence of some Fe is beneficial for processing, such as reducing die soldering in high-pressure die-casting (HPDC) [12]. However, Fe is generally considered to deteriorate mechanical performance, especially the ductility of Si-containing Al-alloys [13-16]. The maximum solubility of Fe in pure solid Al is only 0.04 wt.% [17]. Accordingly, the dissolved Fe almost completely precipitates out in the form of various Fe-containing intermetallic compounds (IMCs) during solidification. For example, more than 17 types of Al-Fe and Al-Fe-Si based IMCs have been reported in Al-alloys [18-19], notable ones being Al_3Fe, $\alpha-Al_8Fe_2Si$ (or $Al_{15}(Fe,Mn)_3Si_2$), $\beta-Al_5FeSi$, $\pi-Al_8Mg_3FeSi_6$, $\delta-Al_4FeSi_2$ and $\gamma-Al_3FeSi$ [10, 17, 20]. The most commonly observed Fe-IMCs in hypo-eutectic Al-Si alloys are $\alpha-$ and $\beta-$IMCs that can acquire different crystal structures, morphologies and compositions, depending on solidification conditions and the alloy composition.

It is generally accepted that needle-like or plate-shaped brittle $\beta-$IMCs allow easy crack nucleation and propagation leading to severe loss of ductility in Fe-containing Al-Si alloys [16, 21-22]. However, it has also been suggested that $\beta-$AlFeSi forms on folded oxide-bifilms entrapped in the melt, with the unbonded oxide surface at the centre of the $\beta-$IMCs being

2

incorrectly considered as cracks [23]. Significant research has been conducted in preventing the formation of β−IMCs during solidification. In particular, the preferential formation of α−IMCs over β−IMCs, which could be achieved by altering solidification conditions or alloying additions, is believed to be less detrimental to the mechanical performance of castings. Research has shown that melt superheating and the use of an increased cooling rate can promote α−IMC formation or refinement of β-platelets [24-26]. However, most investigated IMC conversion from β to α involves chemical modification through the addition of transition elements such as Co, Cr, Mn, Mo, Ni, Cu, V, Mo and W [27-29] or Sr [19, 30-31].

Among these alloying additions, Mn is the most frequently utilised element to counter the Fe impurity by promoting the formation of α−IMCs. Unlike plate-shaped Fe-IMCs such as δ or predominantly β, α−IMCs may not drastically deteriorate ductility. The addition of Mn, however, has been linked with (i) increased sludge (more IMCs) and porosity formation, and (ii) reduced machinability of components [16, 23, 32-33]. Various morphologies of α−IMCs have been observed such as the Chinese-script, blocky, compact, star-like, flower-like, coarse-dendritic or even elongated rods due to the combined complex influences of the cooling rate and Mn content [34]. The addition level of Mn to counter Fe has not been clearly established though a minimum Mn/Fe ratio of 0.5 is often suggested. However, excessive addition of Mn can risk reversing its positive effect on the mechanical properties leading to severe loss in strength and ductility [30].

An alternative to chemical approach is to apply physical fields during solidification to manipulate the evolving microstructure. Direct application of high-intensity ultrasound has shown primary grain refinement [35-38], eutectic modification [39-41], and alteration of the morphology and type of Fe-IMCs in high-Si containing Al-alloys [40-47]. Most of these studies involved hyper-eutectic Al-Si alloys where ultrasonication affected the morphology and transformation kinetics between plate-like δ−IMCs and β−IMCs. A recent investigation of Al-17Si-2Fe alloy (in wt.% henceforth) established that increasing Mn content alone without ultrasonication led to severe macro-segregation and formation of coarse IMCs, while not all δ−IMCs and β−IMCs transformed into desirable α−IMCs [48]. However, the combination of ultrasonication with Mn-addition was able to avoid all the issues and resulted in the formation of fine polyhedral α−IMCs [48]. The possibility to simultaneously refine the primary grain structure and modify the nature and morphologies of IMCs under ultrasonication is highly attractive and difficult to achieve by the chemical approaches explored so far.

The objective of this study is to investigate the effect of ultrasonication on the nature and morphology of Fe-IMCs in recycled-Al alloys where alloying elements are leaner than in traditional Al-Si casting alloys. Recycled Al-alloy compositions may vary significantly depending on the scrap used. Wrought Al-alloys account for two thirds of all Al-alloys in use [49]. 6000 series being one of the most widely used is expected to be the major scrap used for recycling. Yet only 20% of the scrap is recycled into wrought products due to the high impurity sensitivity of the ductile Al-Mg-Si alloys [49]. In 6000 series alloys, the Mg and Si content varies between 0.6-1.4wt.%. However, addition of cast Al-Si-Mg alloy (300 series) scrap can significantly increase the Si and Mg content in the recycled alloy. Accordingly, an experimental alloy with 2wt.% of Mg and Si (above the limit used in commercial 6000 series) is used to represent the recycled-Al alloy, while the Fe content is kept moderately high to investigate the effect on Fe-IMCs. Inspired by the combined benefits of ultrasonication and Mn-addition [48], two Mn-addition levels were used. The nature of the Fe-containing IMCs formed and the effectiveness of ultrasonication in modifying them are investigated and the origin of microstructural modification is explored.

2. Materials and methods

Alloys of nominal composition Al-2Si-2Mg-1.2Fe-xMn (x =0.5 and 1%) were prepared in a clay-graphite crucible in an electric resistance furnace. Measured amounts of master alloys were melted at 760 ± 3°C, thoroughly mixed, and homogenised for 2 h with intermittent stirring. In this article, Al-2Si-2Mg-1.2Fe-0.5Mn and Al-2Si-2Mg-1.2Fe-1Mn are termed as 0.5Mn and 1.0Mn alloys, respectively. Compositions of the prepared alloys were verified by optical emission spectroscopy.

In each experiment, 450 ± 15 g of the alloy melt was taken out in a clay-graphite crucible preheated to 740 ± 3°C, placed on a refractory slab and ultrasonicated while cooling naturally in air. Ultrasonication (at 20 kHz frequency and 25 μm amplitude) was performed using a Nb radiator (horn) immersed to 1-2 cm below the melt surface. Figs. 1(a-c) schematically illustrates the three different ultrasound application regimes, while Fig. 1(d) shows the corresponding ultrasonication range on a cooling curve. A thermocouple, connected to a multichannel data logger, was placed below the submerged radiator to record the cooling process. The radiator was preheated to 450 °C before immersion into the melt to avoid solid built up on its surface. Experiments were repeated to ensure reproducibility and samples were solidified under identical conditions, but without ultrasonication, for comparison.
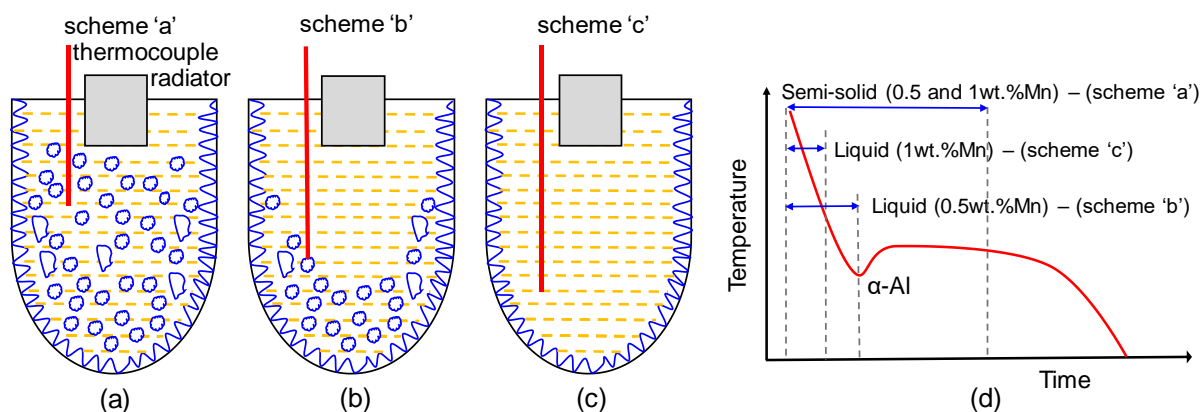
Fig. 1 *Schematic representation of ultrasonication: (a) ultrasonication continued into the semi-solid region (scheme 'a'), (b) ultrasonication continued till maximum nucleation undercooling for primary-Al (scheme 'b'), (c) ultrasonication terminated prior to primary-Al nucleation (scheme 'c'), and (d) ultrasonication regimes highlighted on the cooling curve.*

The nucleation undercooling has been shown to differ with and without ultrasonication [38, 40]. Therefore, it is difficult to predetermine the withdrawal of the ultrasound horn prior to or just after primary-Al nucleation. Experiments involving ultrasonication from the molten to the mushy state (scheme 'a' in Fig. 1) were conducted first and the nucleation undercooling was recorded from the cooling curves. On this basis, for anticipated ultrasound withdrawal just after primary-Al nucleation, the horn was withdrawn on reaching the maximum undercooling (scheme 'b' in Fig. 1). For experiments involving ultrasonication in the fully liquid state, the horn was withdrawn well before reaching the maximum undercooling (scheme 'c' in Fig. 1). A characteristic noise is observed in the cooling curves recorded under ultrasonication compared with a smooth curve recorded without ultrasonication. This allowed verification of the point of ultrasonication withdrawal from the cooling curves measured during the experiments.

The solidified ingots (Ø 70 mm, height 75–80 mm) were sectioned longitudinally in the middle; then ground and polished through standard metallographic techniques using SiC abrasive papers and 0.25 μm colloidal silica suspension. Un-etched samples were examined using a ZEISS Axioscop2 MAT optical microscope equipped with an AxioVision image capture and analysis module. To enhance the grain structure, samples were also anodised in Barker's reagent (7 ml 48% HBF_4, 93 ml H_2O) at 20 V for 70 s using a stainless-steel cathode. Selected samples were deep-etched using 37% HCl for 90 s to investigate the morphology of

5

the IMCs. Phase identification was carried out using a FEI Quanta Field Emission Gun (FEG) scanning electron microscope (SEM) equipped with energy dispersive spectroscopy (EDS) and a PANalytical X-ray diffractometer (XRD) using Cu target. Phase transformations within the solidification range of the alloys were investigated using a NETZSCH STA449 F3 differential scanning calorimeter (DSC). In each DSC experiment, approximately 20 mg sample was heated and cooled between 350 °C to 750 °C at 5 °Cmin^{-1}.

3. Results

3.1 Solidification microstructure

Figures 2(a, b) present the XRD patterns obtained from the conventional and ultrasonicated samples for the 0.5Mn and 1.0Mn alloys. No difference was detected with and without ultrasonication. Primary-Al constitutes the major phase with small amounts of α–$Al_{15}(Fe,Mn)_3Si_2$ IMC and other IMCs, Mg_2Si and π–$Al_8(Fe,Mg)_3Si_6$.
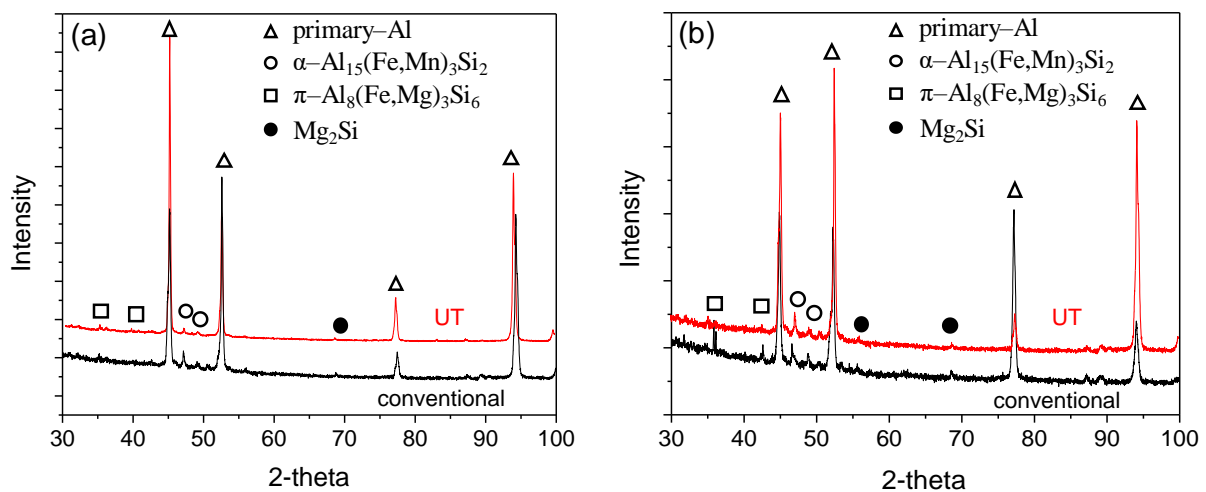

Fig. 2 *XRD patterns from samples solidified conventionally and under ultrasonication (UT) in, (a) 0.5 wt.% Mn alloy and (b)1 wt.% Mn alloy.*

The as-cast microstructures without ultrasonication consist of primary-Al dendrites (marked 'A' in Fig. 3) interspersed with α–$Al_{15}(Fe,Mn)_3Si_2$ (light-grey phase marked 'B') and small amounts of Mg_2Si (black phase marked 'C') and π–$Al_8(Fe,Mg)_3Si_6$ (marked 'D'). There is no perceptible difference in microstructure between the Mn addition levels. No plate-shaped β–$Al_5(Fe,Mn)Si$ IMCs were observed. Previous research has indicated that a minimum Mn/Fe ratio of 0.5 is required to fully convert β–IMCs into α–IMCs [25]. The present results agree well for the high-Mn alloy with Mn/Fe ratio above 0.8. A recent investigation in Al-8Si-

0.35Mg alloys with varying Fe and Mn content has indicated that formation of β−IMCs and α−IMCs are co-dependent on both the Mn/Fe ratio and the cooling rate [50]. For the cooling rates experienced in the present investigation (0.3°C/s), a minimum Mn/Fe ratio of 1.0 is suggested to suppress β−IMC formation [50]. However, β−IMC appears to be suppressed even in the low Mn alloy with a Mn/Fe ratio of ~ 0.4. It appears that intermetallic formation may also depend on the Si level (present alloys are leaner in Si compared to previous work) and the presence of other alloying elements, especially Mg, that forms intermetallic compounds with Si. Both Mn and Mg has been shown to suppress the formation temperature of β−IMC [50]. Prior nucleation of α−IMC and Mg_2Si may have prevented β−IMC formation in the present low-Si high-Mg alloys. In contrast, prior research on β−IMC and δ−IMC formation predominantly features Si-rich Al-Si-Fe alloys. More research on the effect of different alloying elements on the nature of Fe-IMC is necessary to form a clear understanding of their formation. Nevertheless, the large complex dendrites of α−IMCs are always undesired due to their linkage to porosity, sludge formation and reduced machinability.
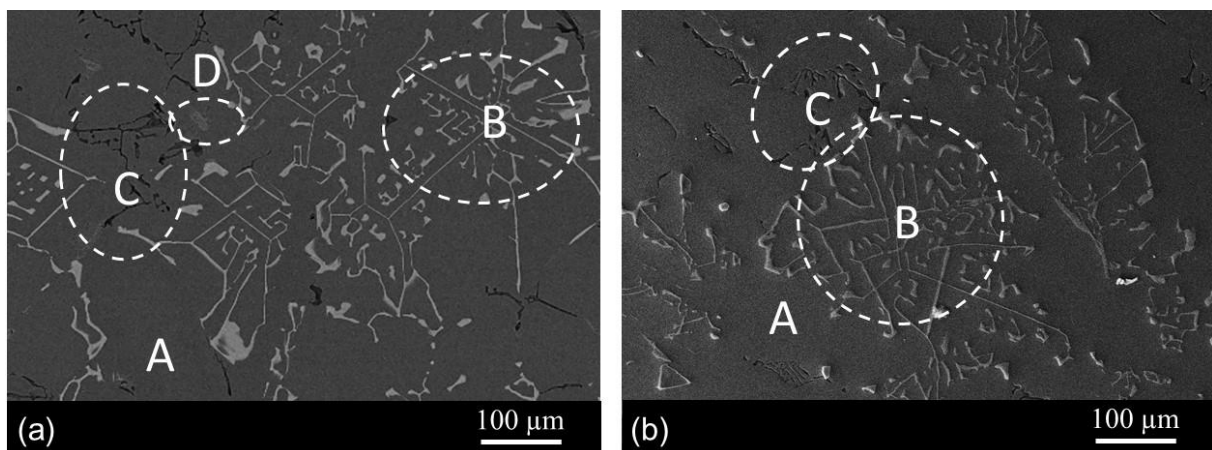

Fig. 3   *SEM images from (a) 0.5 wt.% Mn alloy and (b) 1 wt.% Mn alloy cooled naturally from 740 °C. The matrix phase is primary-Al grains (marked A). Different intermetallic phases observed are, Chinese-script type α−$Al_{15}(Fe,Mn)_3Si_2$ (light grey phase marked B), Mg_2Si (black phase marked C) and π−$Al_8(Fe,Mg)_3Si_6$ (marked D).*

3.2 Effect of ultrasonication on the primary-Al grain structure

Figures 4 and 5 present polarised light micrographs from the 0.5Mn and 1.0Mn alloys, respectively, with and without ultrasonication. Figs. 4a and 5a show fully-grown dendritic primary-Al grains up to several millimetres in size in the conventionally solidified ingots. Ultrasonication resulted in noticeable refinement of the primary-Al grain structure. However, both the extent of refinement and the morphology were found to depend on the application

regime of ultrasound. When the ultrasound was applied in the superheated liquid but withdrawn prior to primary-Al nucleation (scheme 'c' in Fig.1), the resulting grain structure was refined only marginally. Moreover, the primary-Al grains remained dendritic in nature. This can be observed by comparing Fig. 5c (ultrasonicated) with Fig. 5a (conventional).
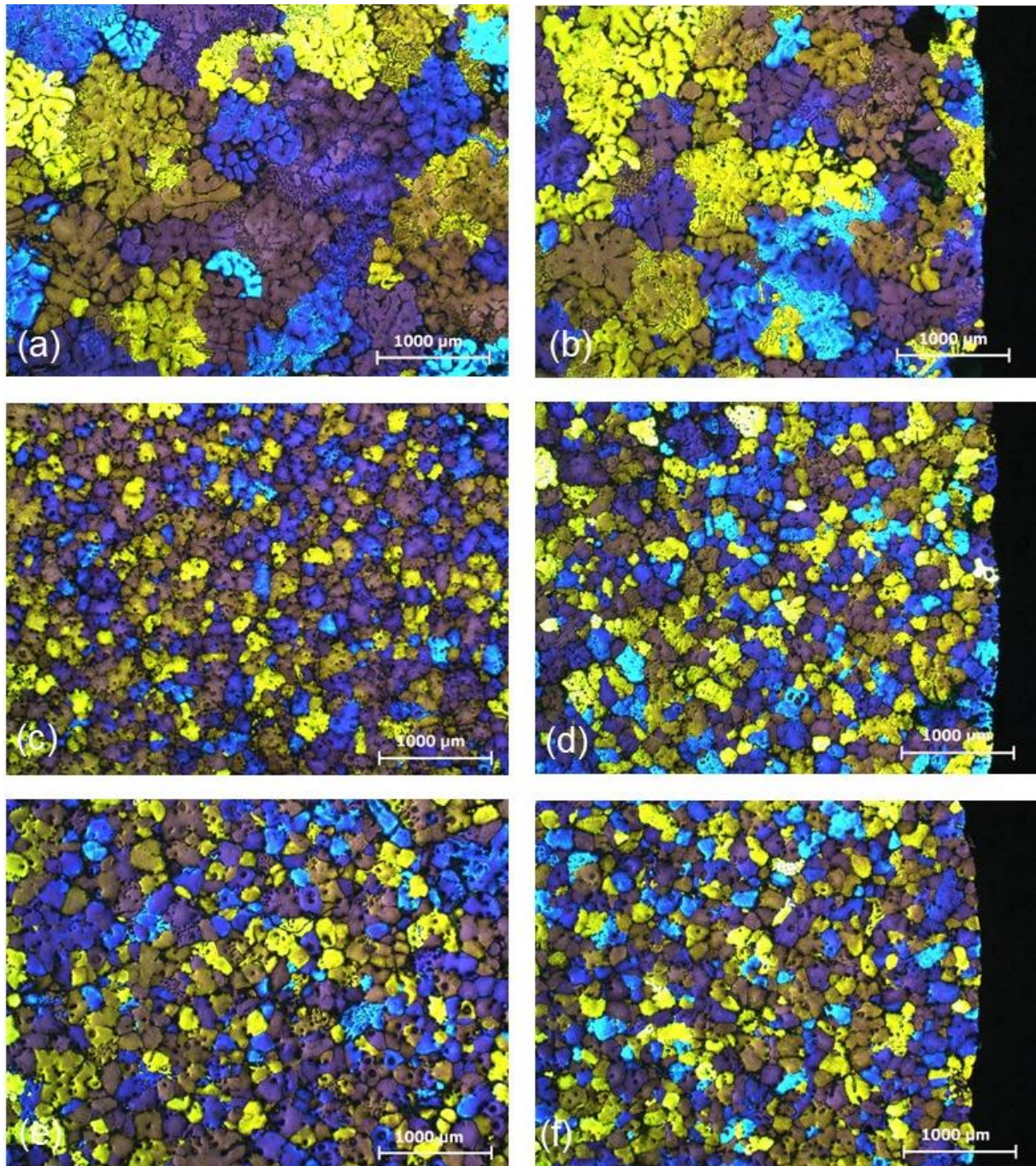

Fig. 4 *Polarised light micrographs from the 0.5 wt.% Mn alloy ingots:(a-b) solidified without ultrasonication, (c-d) under ultrasonication well into the semisolid state (scheme 'a' in Fig. 1d) and (e-f) ultrasonicated till maximum undercooling (scheme 'b' in Fig. 1d). Images on the left are from the centre of the ingot, while those on the right are from the edge of the ingot.*
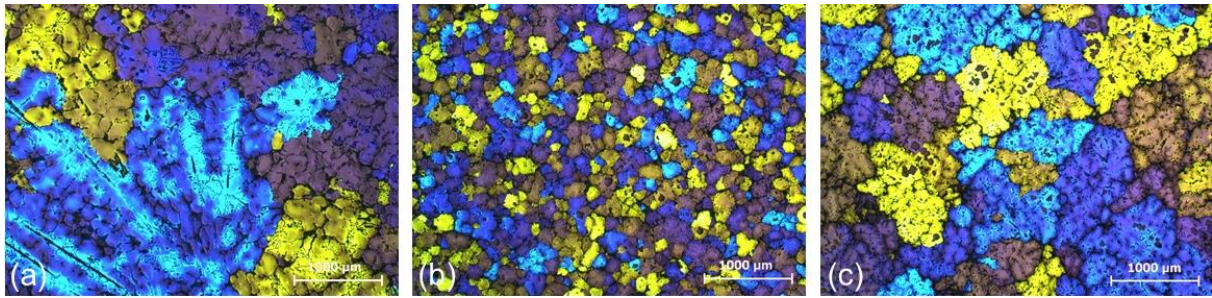
Fig. 5 *Polarised light micrographs from the centre of 1.0 wt.% Mn alloy ingots: (a) solidified without ultrasonication, (b) under ultrasonication well into the semisolid state (scheme 'a' in Fig. 1d) and (c) ultrasonicated in the liquid state prior to primary-Al nucleation (scheme 'c' in Fig. 1d).*

In contrast, continued ultrasonication into the semisolid stage (scheme 'a' in Fig. 1) promoted a significantly refined non-dendritic primary-Al grain structure. This is illustrated in Figs. 4c and 5b from the centre of the ingot, right below the ultrasound horn. The entire ingot exhibited a refined equiaxed grain structure. Fig. 4d shows similar morphology and grain size near the crucible wall as in the area near the horn (Fig. 4c). Withdrawing ultrasound just after reaching the maximum undercooling (scheme 'b' in Fig. 1) did not promote dendritic growth. Figs. 4e and 4f show refined non-dendritic grains near the horn and the crucible wall, respectively. These observations suggest that the refined equiaxed grains are a result of primary-Al nucleation under ultrasonication. In contrast, grain refinement is marginal with dendritic solidification when the ultrasound is withdrawn prior to primary-Al nucleation. Also, further ultrasonication after the primary-Al grain nucleation is unnecessary to retain the refined non-dendritic grain structure.

3.3 Effect of ultrasonication on the morphology of intermetallic phases

Figures 6 and 7 present solidification morphologies of the IMCs in the 0.5Mn and 1.0Mn alloys, respectively. Figs. 6a and 7a illustrate the overall distribution while Figs. 6b and 7b show the morphologies of the IMCs in the base ingots without ultrasonication. The Chinese-script α–$Al_{15}(Fe,Mn)_3Si_2$ with sizes ranging between 300 and 600 μm is the predominant IMC phase dispersed within the Al matrix. Blocky α–$Al_{15}(Fe,Mn)_3Si_2$ IMCs have been reported previously in Al-Si alloys with high Mn contents [25, 48]. However, no blocky α–IMC formation was observed from the increased Mn-content in the present lean alloy.
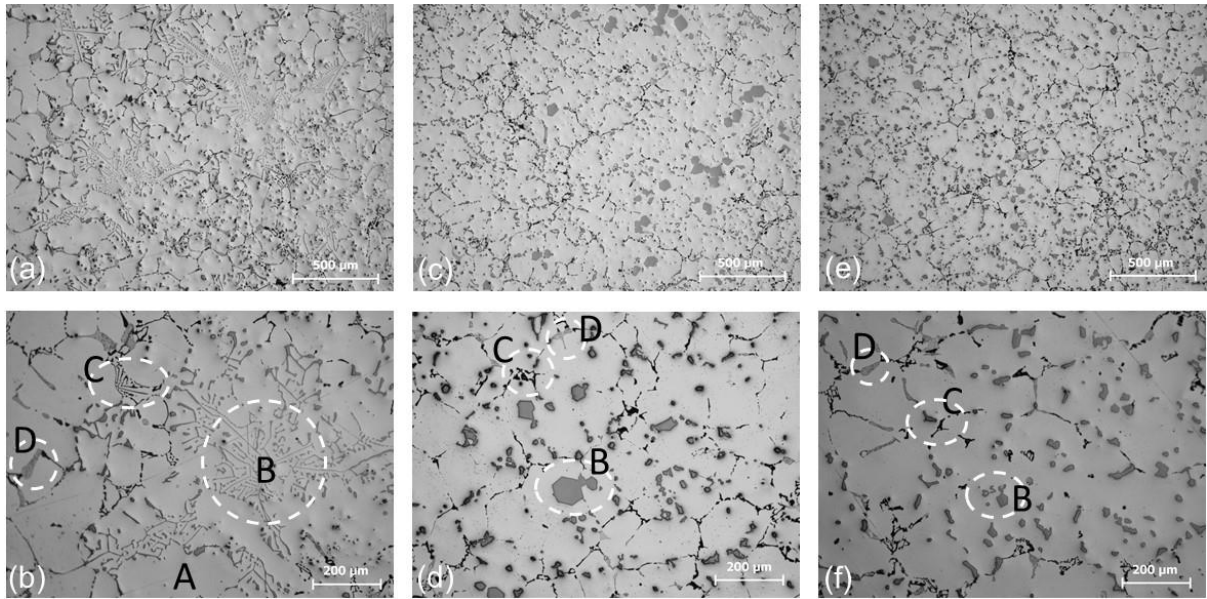
Fig. 6 *Optical micrographs from the 0.5 wt.% Mn alloy samples: (a-b) solidified without ultrasonication, (c-d) ultrasonicated well into the semisolid state (scheme 'a' in Fig. 1d) and (e-f) ultrasonicated till maximum undercooling (scheme 'b' in Fig. 1d). Nature of the intermetallic phases marked in the micrographs is explained in Fig. 3.*
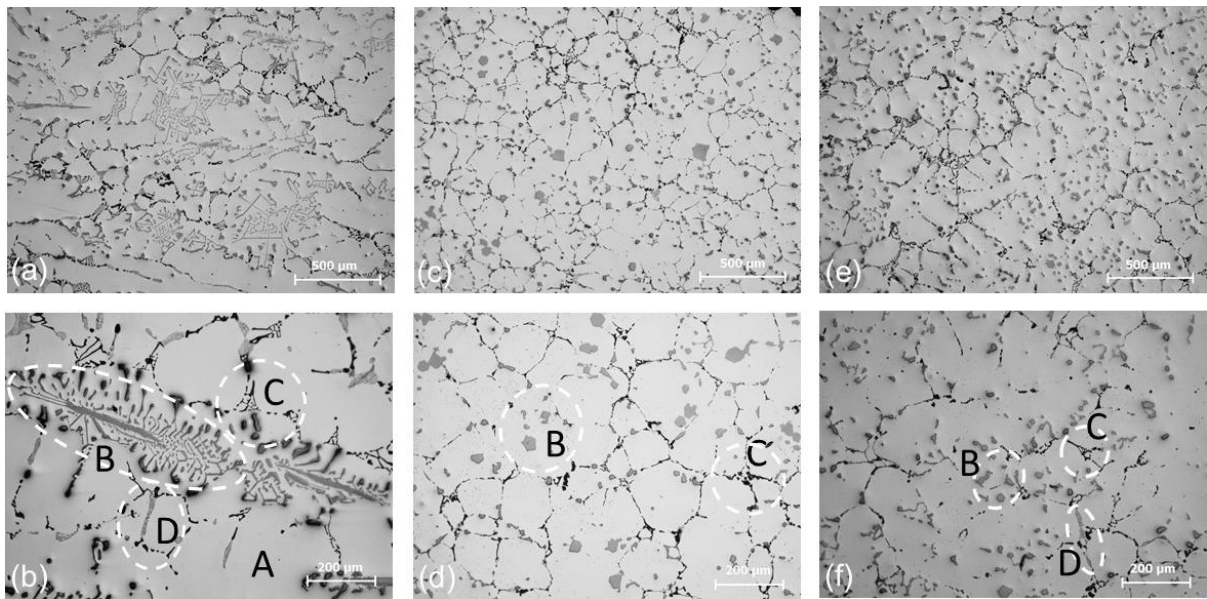

Fig. 7 *Optical micrographs from the 1.0 wt.% Mn alloy samples: (a-b) solidified without ultrasonication, (c-d) ultrasonicated well into the semisolid state (scheme 'a' in Fig. 1d) and (e-f) ultrasonicated in the liquid state (scheme 'c' in Fig. 1d). Nature of the intermetallic phases marked in the micrographs is explained in Fig. 3.*

Ultrasonication produced substantial morphological transformation and refinement of the α–IMCs in both alloys. EDS analysis of seven random α–IMCs (Table 1) indicates that they are chemically identical irrespective of ultrasonication. Ultrasonication till semisolid state

10

(scheme 'a' in Fig. 1d) produced well-dispersed refined polygonal α–IMCs of 20-70 µm in particle size (Figs. 6c and 6d). Withdrawing ultrasound following primary-Al nucleation (scheme 'b' in Fig. 1d) still produced refined polygonal α–IMCs of 10-25 µm in size as shown in Figs. 6e and 6f. While their morphology remains compact polygonal, prolonged ultrasonication appears to have slightly coarsened the particles (compare Fig. 6d to 6f). Similar modification of α–Al$_{15}$(Fe,Mn)$_3$Si$_2$ under ultrasonication was observed in the higher Mn alloy as shown in Figs. 7c and 7d. Refined polygonal α–IMCs solidified even when the ultrasonication was terminated before primary-Al nucleation (scheme 'c' in Fig. 1d) as shown in Figs. 7e and 7f. This suggests that α–IMCs nucleated prior to primary-Al before the horn was withdrawn. Similar to the case of the lower Mn alloy, prolonged ultrasonication led to slight coarsening of the particles as evident by comparing Figs. 7d and 7f.

Figures 6 and 7 also indicate minor quantities of Mg$_2$Si and π–Al$_8$(Fe,Mg)$_3$Si$_6$ solidifying in the eutectic areas between primary-Al grains. No major morphological changes were observed for these IMCs. Both of these phases solidified outside the influence of ultrasonication, presumably after the horn was withdrawn. Large scattered eutectic pockets in the conventionally solidified specimen allowed the Mg$_2$Si phase to grow and develop (Figs. 6b and 7b). Under ultrasonication, finer well-distributed eutectic pockets resulted from primary-Al refinement. This has somewhat restricted the growth of Mg$_2$Si into thin particles between the primary-Al grains.

Table 1. *Composition of the Fe-intermetallic phases in conventionally solidified (reference) and ultrasonicated (UT) melts.*

Condition	Chemical composition (at. %)				Fe/Si ratio
	Al	Fe	Si	Mn	
0.5 wt.% Mn Reference	75.4	13.5	7.1	4.1	1.9
0.5 wt.% Mn UT	75.1	13.5	7.6	3.8	1.8
1 wt.% Mn Reference	73.0	12.4	6.5	8.1	1.9
1 wt.% Mn UT	73.7	12.3	6.9	7.1	1.8

3.4 Solidification sequence of phases

To help understand microstructure evolution under ultrasonication, the solidification sequence of the alloys was investigated using computational thermodynamics. Figs. 8a and 8b present

the phase fractions evolved under non-equilibrium solidification for the 0.5 and 1.0Mn alloys, respectively, calculated using a CALPHAD software tool.
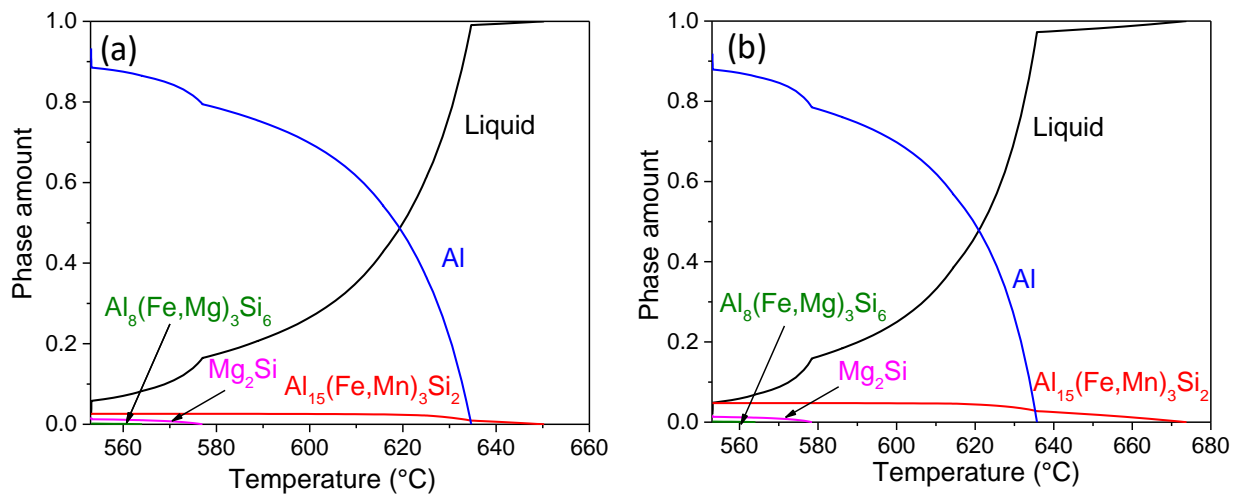

Fig. 8 *Evolution of phase fractions as a function of temperature, as calculated through CALPHAD software, in (a) the 0.5 wt.% Mn and (b) the 1.0 wt.% Mn alloy.*

In the 0.5Mn alloy (Fig. 8a), α–Al_{15}(Fe,Mn)$_3$Si$_2$ starts solidifying at 648 °C and steadily increases till about 623 °C. Primary-Al forms at 634 °C and constitutes the major solidifying phase. The start of Mg_2Si solidification coincides with a sudden increase in the Al fraction at 577 °C, indicating a eutectic reaction involving these phases. π–Al_8(Fe,Mg)$_3$Si$_6$ is the last phase to solidify starting at 564 °C. The calculated phase fractions qualitatively agree with the phases and their content in the microstructure (Figs. 2 and 3). A similar solidification sequence is predicted for the 1.0Mn alloy (Fig. 8b). α–Al_{15}(Fe,Mn)$_3$Si$_2$ solidifies first, albeit at a higher temperature of 672 °C. Primary-Al starts solidifying at 636 °C, followed by a eutectic solidification involving Mg_2Si and Al at 578 °C. π–Al_8(Fe,Mg)$_3$Si$_6$ is the last phase to solidify starting at 561 °C. As with the 0.5Mn alloy, the calculated phase fractions qualitatively agree with the observed microstructure in the 1.0Mn alloy (Figs. 2 and 3).

DSC scans were then compared with the CALPHAD predictions for a more accurate description of the solidification events in both alloys. Figs. 9a and 9b present the DSC traces recorded during heating and cooling of the 0.5 and 1.0% Mn alloys, respectively. Fig. 9a shows three major phase transformations during cooling of the 0.5% Mn alloy from the fully liquid state. Identical transformations are detected during heating, albeit at slightly different temperatures, from the solid to the liquid state. Primary-Al solidification produces the major peak at about 641 °C, followed by two small peaks corresponding to eutectic solidification of

Mg$_2$Si at 578 ^{o}C and π–Al$_8$(Fe,Mg)$_3$Si$_6$ at 554 ^{o}C. The DSC results are in good agreement with the computational thermodynamics predictions of the solidification path. Similar agreement was observed for the 1% Mn alloy where the DSC traces (Fig. 9b) indicate primary-Al nucleation at 640 ^{o}C, followed by eutectic solidification of Mg$_2$Si and π–Al$_8$(Fe,Mg)$_3$Si$_6$ at 580 ^{o}C and 554 ^{o}C, respectively. However, no peaks corresponding to α–Al$_{15}$(Fe,Mn)$_3$Si$_2$ nucleation were detected from the DSC traces. This suggests that nucleation of α–IMCs is not prolific, and the IMCs evolved slowly over a temperature range.

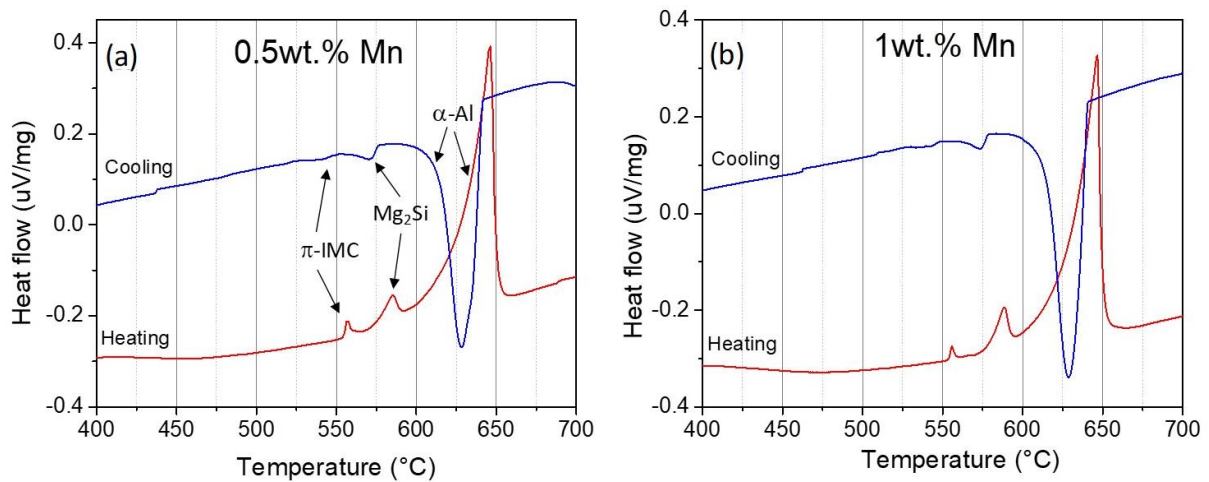Fig. 9 *DSC heat flow curves obtained during heating and cooling of (a) 0.5 wt.% Mn and (b) 1.0 wt.% Mn alloys.*

4. Discussion

4.1 Effect of ultrasonication on the solidifying melt

The effect of ultrasonication on metallic melts has been explained based on cavitation and acoustic streaming [35, 51]. The former involves nucleation, growth and collapse of gas bubbles in the melt (above a cavitation threshold) leading to local shockwave pulses of 1000 atm and microjets of 100 ms^{-1} [52]. Our estimate suggests an ultrasound energy density of 1500 Wcm^{-2} in the present set-up, well above the reported cavitation threshold of 100 Wcm^{-2} in Al melt [38]. Acoustic streaming, from the attenuation of ultrasound in the melt, promotes large-scale steady fluid flow dissipating heat and solute and dispersing nuclei in the melt. Although cavitation is considered responsible for microstructural refinement, the exact mechanism(s) is still debated. Dendrite fragmentation under cavitation and dispersion of fragments through acoustic streaming are thought to contribute to grain refinement [35, 51]. Alternative theories

suggest that heterogeneous nucleation is enhanced from pressure induced shift in freezing point or adiabatic melt cooling at the surface of cavitation bubbles [53-54].
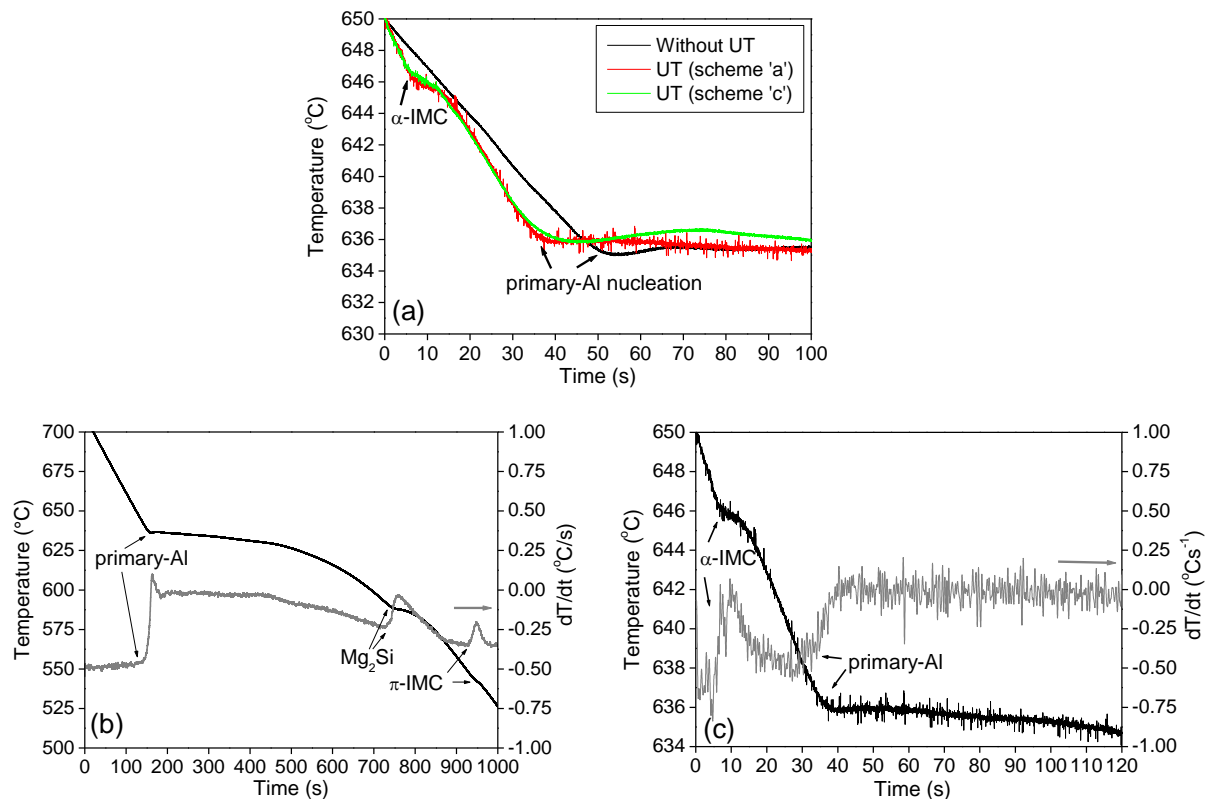

Fig. 10 *Cooling curves measured during the solidification of 0.5 wt.% Mn alloy. (a) shows the cooling curves obtained under different solidification conditions. The time derivative of the cooling curve is superimposed indicating the phase transformations under (b) conventional solidification and (c) ultrasonication (UT).*

Solidification of the 0.5% Mn alloy is examined with the help of cooling curves (Fig. 10a) measured with and without ultrasonication (schemes 'a' and 'c'). The time derivatives of the cooling curves are superimposed on Figs. 10b and 10c for conventional solidification and ultrasonication (scheme 'a'), respectively. The major nucleation events can be identified from the peaks observed in the time derivative of the cooling curve. Under conventional solidification, primary-Al nucleates at 636 °C, eutectic Mg_2Si at 585 °C and π–$Al_8(Fe,Mg)_3Si_6$ at 550 °C. These values agree well with the computational thermodynamics calculation (Fig. 8) and DSC measurements (Fig. 9a). As with the DSC traces, no α–$Al_{15}(Fe,Mn)_3Si_2$ peak could be identified in the cooling curve, indicating insignificant nucleation. The presence of large Chinese-script α–IMCs in the microstructure (Fig. 8) suggests that their morphological evolution occurs predominantly through growth over a temperature range with nucleation playing a trivial role. In contrast, Fig. 10 clearly shows that ultrasonication promoted α–IMC

nucleation with a distinct peak appearing at ~647 °C in the cooling curves. However, growth still plays a major role in its morphological evolution as discussed below.

4.2 Modification of α–Al₁₅(Fe, Mn)₃Si₂ morphology under ultrasonication

Previous work has shown that α–IMCs form through peritectic reaction or, for Si >5wt.%, directly solidifies from the liquid [55]. However, Fig. 10 indicates direct α–IMC solidification under ultrasonication at a lower Si content in the present alloys. It has been reported that α–IMCs nucleate on oxides [34]. Forced wetting of inclusions has been proposed under cavitation [52] and demonstrated in oxide containing metal matrix composite [56]. Therefore, cavitation assisted wetting of oxide films is expected to increase heterogeneous nucleation sites explaining the α–IMC nucleation peak observed under ultrasonication (Fig. 10).

Despite the enhanced nucleation from ultrasonication, the α–IMC fraction is low in the microstructure. This excludes hard (physical contact between particles) or soft impingement (overlapping of solute diffusion fields) during growth. The morphological evolution of a freely growing solid is dictated by the stability of its interface. For diffusion-controlled growth in a supersaturated matrix, the Mullins-Sekerka instability commences at a critical radius

$$r_c = \frac{14\Gamma_D}{(C_\infty - C_0)/C_0}$$

where Γ_D is a capillary constant, and C_0 and C_∞ are the equilibrium concentrations at the interface and original concentration of the matrix, respectively [57]. The critical radius sharply decreases with increasing solute supersaturation ($C_\infty - C_0$) ahead of the interface. For thermal growth in a supercooled melt, the critical radius for instability is given by [57]

$$r_c = \frac{2\Gamma_T(7 + 4k_S/k_L)}{(T_M - T_\infty)/T_M}$$

where Γ_T is another capillary constant, k_S and k_L are thermal conductivities in the solid and the liquid, respectively, and T_M and T_∞ represent the respective melting point (interface temperature) and initial temperature of the melt [57]. The critical radius sharply decreases with increasing thermal undercooling ($T_M - T_\infty$) at the interface. Both thermal (from poor nucleation) and constitutional (from rejected solute at the interface) undercooling are relevant to α–IMC solidification, in isolation or in conjunction, leading to early growth instability.

While the Mullins-Sekerka analysis ignores anisotropic interface energy, α–IMC evolution may involve a significant role of surface energy anisotropy. Phase-field simulation in anisotropic Al-Si system has shown a change in Si growth morphology from faceted to dendritic at large undercooling [58]. Similarly, faceted Sb-doped Ge was shown to develop instability from high interface solute supersaturation [59]. It appears that thermal and solutal driven growth instability is applicable to faceted crystals, although a higher undercooling and/or solute supersaturation is needed for such instability compared to non-faceted particles. Accordingly, freely growing α–IMC particles (and fragments generated under cavitation) are expected to develop dendritically in the melt.
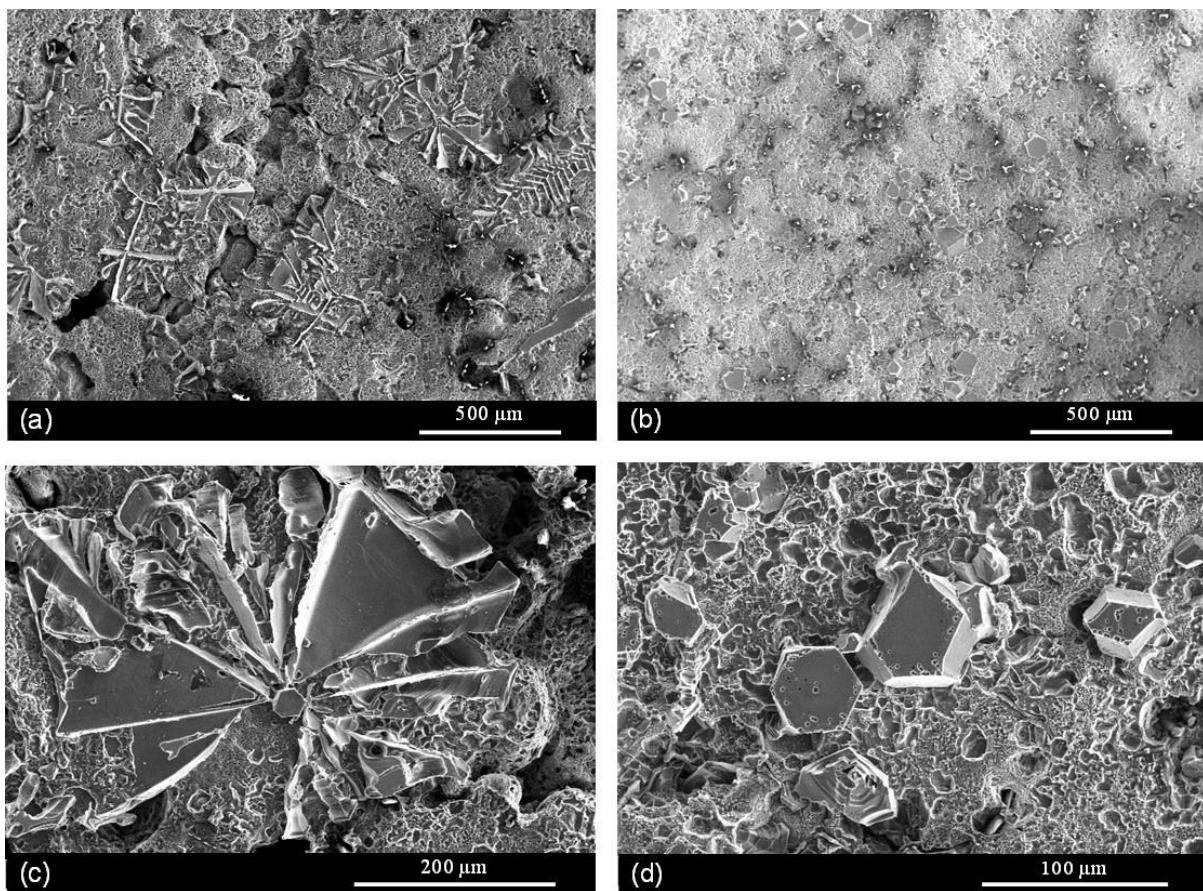

Fig. 11 *Deep-etched microstructure illustrating the morphology of the α-Al(Fe,Mn)Si intermetallics formed (a) without and (b) with ultrasonication. Corresponding high magnification micrographs are presented in (c) for conventional solidification and (d) under ultrasonication.*

The morphology of the α–IMCs is shown in Fig. 11. All α–IMCs in the ultrasonicated sample (Fig. 11b) are polygonal but are the Chinese-script type in the conventionally solidified sample (Fig. 11a). Fig. 11c reveals radial branching of a central polygonal particle leading to a

Chinese-script particle, suggesting early growth instability under conventional solidification. In contrast, the α–IMCs formed under ultrasonication are compact polyhedral bound by facets and devoid of growth instability (Fig. 11d). Note that Fig. 11d is presented at higher magnification than Fig. 11c to highlight the 3D morphologies of the polygonal IMCs. They are significantly finer than the Chinese-script IMCs but much larger than the polyhedral crystals at the centre of Chinese-script IMCs. This signifies that the α–IMCs have grown further without encountering interface instability under ultrasonication. The reasons can be attributed to low interface undercooling from enhanced nucleation and low solute supersaturation from fluid flow during free growth of the α–IMCs under ultrasonication according to the stability theory discussed earlier.

4.3 Refinement of primary-Al grain structure under ultrasonication

Ultrasound induced grain refinement has been extensively investigated for both Al and Mg alloys and explained based on dendrite fragmentation or enhanced nucleation [35-38, 52]. Figures 4 and 5 highlight prolific grain refinement when primary-Al nucleate under ultrasonication (schemes 'a' and 'b'). Fig. 10a shows lower nucleation undercooling for primary-Al under ultrasonication (compared to conventional solidification), suggesting enhanced heterogeneous nucleation. This is consistent with our previous observations in various Al-alloys [38, 40-41]. In contrast, ultrasound withdrawal prior to primary-Al nucleation (scheme 'c') produced dendritic growth with minor grain refinement (compare Fig. 5c against 5a), similar to earlier observation in Al-Cu [60, 61]. This suggests that forced wetting of substrates alone is insufficient to account for the enhanced primary-Al nucleation (Fig. 10) under ultrasonication.

There is no perceptible difference in the refinement levels between schemes 'a' (Figs. 4c,d) and 'b' (Figs. 4e,f) suggesting fragmentation of primary-Al in the semisolid state is negligible. Enhanced nucleation has also been explained from the pressure-induced increase in the freezing point under cavitation [53-54]. The increase in freezing point can activate the less potent substrates wetted under cavitation, such as the oxides, through increased thermal undercooling [38, 40]. This explains why primary-Al refinement is significant under ultrasonication but marginal when ultrasonication is terminated prior to Al-solidification in the present study. Fig. 10a also shows recalescence is minimal when ultrasonication continued through nucleation but prominent when withdrawn prior to primary-Al nucleation. It can be

explained from effective dissipation of latent heat under intense convection and may further increase refinement by prolonging nucleation.

5. Conclusions

The solidification microstructure formed in custom Al-2Si-2Mg-1.2Fe-xMn (x =0.5 and 1 wt.%) alloys, representative of recycled-Al, is examined and compared in the presence and absence of ultrasonication under identical natural air-cooling conditions.

The microstructure consists of primary-Al grains with intergranular α–Al$_{15}$(Fe,Mn)$_3$Si$_2$ and minor amounts of Mg$_2$Si and π–Al$_8$(Fe,Mg)$_3$Si$_6$ intermetallics in agreement with computational thermodynamics predictions. Ultrasonication produced no noticeable change in each constituent phase fraction.

Coarse dendritic primary-Al grains in the base ingots were drastically refined to compact grains when the melt was ultrasonicated until or beyond the primary-Al nucleation stage during cooling. However, terminating ultrasonication prior to primary-Al nucleation reverted to dendritic grain formation with marginal refinement.

Cooling curves from the Al-2Si-2Mg-1.2Fe-0.5Mn alloy indicate a noticeable reduction in the primary-Al nucleation undercooling under ultrasonication. In addition, the prominent recalescence peak observed following primary-Al nucleation in the absence of ultrasonication was effectively eliminated when solidified under ultrasonication.

Coarse Chinese-script α–Al$_{15}$(Fe,Mn)$_3$Si$_2$ formed in the absence of ultrasonication, but was converted to refined polygonal particles bound by flat surfaces under ultrasonication. Distinct α–Al$_{15}$(Fe,Mn)$_3$Si$_2$ nucleation peak was observed only under ultrasonication in the Al-2Si-2Mg-1.2Fe-0.5Mn alloy cooling curve, suggesting that ultrasonication promoted nucleation of the intermetallic.

Chinese-script α–Al$_{15}$(Fe,Mn)$_3$Si$_2$ IMCs develop from initially polygonal particles due to growth instability from undercooling and solute supersaturation. Their modification to much refined polygonal particles by ultrasonication results from the enhanced nucleation along with growth stabilisation due to solute homogenisation at the solid-liquid interface.

Acknowledgements

References

[1]   A.L. Greer, P.S. Cooper, M.W. Meredith, W. Schneider, P. Schumacher, J.A. Spittle, A. Tronche, Grain refinement of aluminium alloys by inoculation, Adv. Eng. Mater. 5 (2003) 81-91.

[2]   B.S. Murty, S.A. Kori, M. Chakraborty, Grain refinement of aluminium and its alloys by heterogeneous nucleation and alloying, Int. Mater. Rev. 47 (2002) 3-29.

[3]   S.Z. Lu, A. Hellawell, Modification of Al-Si alloys: Microstructure, thermal analysis, and mechanisms, JOM, 47(1995) 38-40.

[4]   J. Campbell, M. Tiryakioğlu, Review of effect of P and Sr on modification and porosity development in Al–Si alloys, Mater. Sci. Tech. 26 (2010) 262-268.

[5]   G. Gaustad, E. Olivetti, R. Kirchain, 'Improving aluminum recycling: A survey of sorting and impurity removal technologies', Resour. Conserv. Recycl. 58 (2012) 79-87.

[6]   S.K. Das, 'Designing aluminium alloys for a recycling friendly world', Mater. Sci. Forum 519–521 (2006) 1239–1244.

[7]   V. Kevorkijan, 'Challenges and advanced of recycling wrought aluminium alloys from lower grade of metallurgically clean scrap', Mater. Technol. (MTAEC9) 47 (2013) 13–23.

[8]   D. Paraskevas, K. Kellens, W. Dewulf, J.R. Duflou, 'Environmental modelling of aluminium recycling: a Life Cycle Assessment tool for sustainable metal management', J. Cleaner Prod. 105 (2015) 357-370.

[9]   K. Nakajima, O. Takeda, T. Miki, K. Matsubae, S Nakamura, T. Nagasaka, 'Thermodynamic analysis of contamination by alloying elements in aluminum recycling', Environ. Sci. Technol. 44 (2012) 5594-5600.

[10]   N.A. Belov, A.A. Aksenov, D.G. Eskin, Iron in Aluminium Alloys: Impurity and Alloying Elements, CRC Press, London, 2002

[11] K. Liu, X. Cao, X-G. Chen, Solidification of Iron-Rich Intermetallic Phases in Al-4.5Cu-0.3Fe Cast Alloy. Metall. Mater. Trans. A 42 (2010) 2004-2016.

[12] L. Wang, M. Makhlouf, D. Apelian, Aluminium die casting alloys: alloy composition, microstructure, and properties-performance relationships. Int. Mater. Rev. 40 (1995) 221–238.

[13] I. Polmear, Light Alloys: From Traditional Alloys to Nanocrystals, 4th Ed. Butterworth-Heinemann, 2005.

[14] J. Davis, ASM Specialty Handbook: Aluminum and Aluminum Alloys, ASM International, 1993.

[15] T.O. Mbuya, B.O. Odera, S.P. Ng'ang'a, Influence of iron on castability and properties of aluminium silicon alloys: literature review. Inter. J. Cast Metals Res. 16 (2003) 451-465.

[16] J.A. Taylor, Iron-Containing Intermetallic Phases in Al-Si Based Casting Alloys, Procedia Mater Sci. 1 (2012) 19-33.

[17] S.J. Maggs, Intermetallic Phase Selection in Dilute AI-Fe-Si alloys. PhD thesis, The University of Leeds, 1996.

[18] V.G. Rivlin, G.V. Raynor, 4: Critical evaluation of constitution of aluminium-iron-silicon system, Int. Metall. Rev. 3 (1981) 133-152.

[19] M.V. Kral, P.N.H. Nakashima, D.R.G. Mitchell, Electron microscope studies of Al-Fe-Si intermetallics in an A1-11 pct Si alloy, Metall. Mate. Trans. A 37 (2006) 1987-1997.

[20] L.F. Mondolfo, Aluminium Alloys: Structure and Properties, Butterworth, London, 1976.

[21] S. Shivkumar, L. Wang, D. Apelian, Molten metal processing of advanced cast aluminum alloys, JOM, 43 (1991) 26–32.

[22] Z. Ma, A.M. Samuel, H.W. Doty, S. Valtierra, F.H. Samuel, Effect of Fe content on the fracture behaviour of Al–Si–Cu cast alloys, Mater. Des. 57 (2014) 366–373.

[23] X. Cao, J. Campbell, Morphology of β-Al5FeSi Phase in Al-Si Cast Alloys, Mater. Trans. 47 (2006) 1303-1312.

[24] L.A. Narayanan, F.H. Samuel, J.E. Gruzleski, Crystallization behavior of iron-containing intermetallic compounds in 319 aluminum alloy, Metall. Mater. Trans. A, 25 (1994) 1761-1773.

[25] Z. Zhang, H. Tezuka, E. Kobayashi, T. Sato, Effects of the Mn/Fe ratio and cooling rate on the modification of Fe intermetallic compounds in cast A356 based alloy with different Fe contents, Mater. Trans. 54 (2013) 1484-1490.

[26] Y. Zhang, Y. Liu, Y. Han, C. Wei, Z. Gao. The role of cooling rate in the microstructure of Al–Fe–Si alloy with high Fe and Si contents, J Alloys Compd. 473 (2009) 442-445.

[27] C.M. Allen, K.A.Q. O'Reilly, B. Cantor, P.V. Evans, Intermetallic phase selection in 1XXX Al alloys, Prog. in Mater. Sci. 43 (1998) 89–170.

[28] M. Mahta, M. Emamy, A. Daman, A. Keyvani, J. Campbell, Precipitation of Fe rich intermetallics in Cr- and Co-modified A413 alloy, Int. J. Cast Metals Res. 18 (2005) 73–79.

[29] T. Gao, K. Hu, L. Wang, B. Zhang, X. Liu, Morphological evolution and strengthening behavior of α-Al(Fe,Mn)Si in Al–6Si–2Fe–xMn alloys, Results in Physics, 7 (2017) 1051–1054.

[30] A.M.A. Mohamed, A.M. Samuel, F.H. Samuel, H.W. Doty, Influence of additives on the microstructure and tensile properties of near-eutectic Al–10.8%Si cast alloy, Mater. Des. 30 (2009) 3943–3957.

[31] P. Ashtari, H. Tezuka, T. Sato, influence of Sr and Mn additions on intermetallic compound morphologies in Al-Si-Cu-Fe cast alloys, Mater. Trans. 44 (2003) 2611-2616.

[32] P.N.Crepeau, Effect of iron in Al–Si alloys: a critical review. AFS Trans. 103 (1995) 361–366.

[33] A. Bjurenstedt, S. Seifeddine, A.E.W. Jarfors, The Effects of Fe-Particles on the Tensile Properties of Al-Si-Cu Alloys, Metals 6 (2016) 314.

[34] A. Bjurenstedt, D. Casari, S. Seifeddine, R.H. Mathiesen, A.K. Dahle, In-situ study of morphology and growth of primary α-Al(FeMnCr)Si intermetallics in an Al-Si alloy, Acta Materialia 130 (2017) 1-9.

[35] G.I. Eskin, D.G.Eskin, Ultrasonic Treatment of Light Alloy Melts. Second Edition. CRC Press 2017.

[36] A. Ramirez, M. Qian, B. Davis, T. Wilks, D.H. StJohn, Potency of high-intensity ultrasonic treatment for grain refinement of magnesium alloys. Scripta Mater. 59 (2008) 19-22.

[37] M. Qian, A. Ramirez, A. Das and D.H. StJohn, The effect of solute on ultrasonic grain refinement of magnesium alloys, J. Crystal Growth, 312 (2010) 2267-2272.

[38] H.R. Kotadia, M. Qian, D.G. Eskin and A. Das, On the microstructural refinement in commercial purity Al and Al-10 wt% Cu alloy under ultrasonication during solidification, Mater. Des. **132** (2017) 266-274.

[39] X. Jian, T.T. Meek, Q. Han, Refinement of eutectic silicon phase of aluminum A356 alloy using high-intensity ultrasonic vibration, Scripta Mater. 54 (2006) 893–896.

[40] A. Das, H.R. Kotadia, Effect of high-intensity ultrasonic irradiation on the modification of solidification microstructure in a Si-rich hypoeutectic Al–Si alloy, Mater. Chem. Phys. 125 (2011) 853-859.

[41] H.R. Kotadia, A. Das, Modification of solidification microstructure in hypo- and hyper-eutectic Al–Si alloys under high-intensity ultrasonic irradiation, J. Alloys Comp. 620 (2015) 1-4.

[42] J. Barbosa, H. Puga, J. Oliveira, S. Ribeiro, M. Prokic, Physical modification of intermetallic phases in Al-Si-Cu alloys, Mater. Chem. Phys. 148 (2014) 1163-1170.

[43] Y. Osawa, S. Takarnori, T. Kimura, K. Minagawa, H. Kakisawa, Morphology of intermetallic compounds in Al-Si-Fe alloy and its control by ultrasonic vibration, Mater. Trans. 48 (2007) 2467-2475.

[44] G. Zhong, S.S. Wu, H.W. Jiang, P. An, Effects of ultrasonic vibration on the iron containing intermetallic compounds of high silicon aluminum alloy with 2% Fe, J. Alloys. Compd. 492 (2010) 482-487.

[45] C. Lin, S. Wu, S. Lü, P. An, L. Wan, Effects of ultrasonic vibration and manganese on microstructure and mechanical properties of hypereutectic Al–Si alloys with 2%Fe, Intermetallics 32 (2013) 176-183.

[46] Y. Zhang, J. Jie, Y. Gao, Y. Lu, T. Li, Effects of ultrasonic treatment on the formation of iron-containing intermetallic compounds in Al-12%Si-2%Fe alloys, Intermetallics 42 (2013) 120-125.

[47] C.J. Todaro, M.A. Easton, D. Qiu, G. Wang, D.H. StJohn, and M. Qian, The Effect of Ultrasonic Melt Treatment on Macro-Segregation and Peritectic Transformation in an Al-19Si-4Fe Alloy, Metall. Mater Trans. A, 48A (2017) 5579-5590.

[48] C.J. Todaro, M.A. Easton, D. Qiu, G. Wang, D.H. StJohn, M. Qian, Effect of ultrasonic melt treatment on intermetallic phase formation in a manganese-modified Al-17Si-2Fe alloy, J. Mater. Proc. Tech. 271 (2019) 346–356.

[49] D. Raabe, C. Cem Tasan, E.A. Olivetti, Strategies for improving the sustainability of structural metals, Nature, 575 (2019) 64-74.

[50] E. Cinkilic, C.D. Ridgeway, X. Yan, A.A. Luo, A formation map of iron-containing intermetallic phases in recycled cast aluminium alloys, Metall. Mater. Trans. A, 50A (2019) 5945-5956.

[51] S.V. Komarov, M. Kuwabara, O.V. Abramov, High Power ultrasonics in pyrometallurgy: current status and recent development, ISIJ International 45 (2005) 1765-1782.

[52] G.I. Eskin, Broad prospects for commercial application of the ultrasonic (cavitation) melt treatment of light alloys, Ultrasonics Sonochemistry, 8 (2001) 319-325.

[53] B. Chalmers, Principles of Solidification, John Wiley & Sons, NY, 1964, pp. 86-89.

[54] J.D. Hunt, K.A. Jackson, Nucleation of Solid in an undercooled liquid by cavitation, J. Appl. Phys. 37 (1966) 254-257.

[55] M. Warmuzek, K. Rabczak, J. Sieniawski, The course of the peritectic transformation in the Al-rich Al–Fe–Mn–Si alloys, J. Mater. Proc. Tech. 162–163 (2005) 422–428.

[56] Y. Tsunekawa, H. Suzuki, Y. Genma, Application of ultrasonic vibration to in situ MMC process by electromagnetic melt stirring, Mater. Des. 22 (2001) 467-472.

[57] W.W. Mullins, R.F. Sekerka, Morphological Stability of a Particle Growing by Diffusion or Heat Flow, Journal of Applied Physics 34, (1963) 323-329.

[58] P.C. Bollada, P.K. Jimack, A.M. Mullis, Faceted and dendritic morphology change in alloy solidification, Computational Materials Science 144 (2018) 76–84.

[59] E. Balikci, A. Deal, R. Abbaschian, S.V. Bykova, V.D. Golyshev, M.A. Gonik, V.B. Tsvetovsky, M.P. Marchenko, I.V. Frjazinov, A study on the morphological stability of faceted interfaces in antimony-doped germanium single crystals grown by the axial heat processing method, Cryst. Growth & Des. 4 (2004) 377-381.

[60] G. Wang, M.S. Dargusch, M. Qian, D.G. Eskin, D.H. StJohn, The role of ultrasonic treatment in refining the as-cast grain structure during the solidification of an Al–2Cu alloy, J Cryst. Growth, 408 (2014) 119-124.

[61] G. Wang, Q. Wang, N. Balasubramani, M. Qian, D.G. Eskin, M.S. Dargusch, D.H. StJohn, The role of ultrasonically induced acoustic streaming in developing fine equiaxed grains during the solidification of an Al-2pct Cu Alloy, Metall. Mater. Trans. A, 50A (2019) 5253-5263.